Coexistence of checkerboard and quasiparticle interference modulations in $Bi_2Sr_2CaCu_2O_{8+x}$ studied by scanning tunneling microscopy/spectroscopy

Shusei Mizuta,[1,*] Migaku Oda,[1,†] Naoki Momono,[2] Hiroyuki K. Yoshida,[1] and Masayuki Ido[1]
[1]*Department of Physics, Faculty of Science, Hokkaido University, Kita 10 Nishi 8, Sapporo 060-0810, Japan*
[2]*Department of Applied Sciences, Muroran Institute of Technology, 27-1 Mizumoto-cho, Muroran 050-8585, Japan*

(Received 11 September 2020; revised 22 October 2020; accepted 22 October 2020; published 23 November 2020; corrected 24 December 2020)

We performed scanning tunneling microscopy/spectroscopy measurements in the superconducting state of underdoped $Bi_2Sr_2CaCu_2O_{8+x}$, and demonstrated that the checkerboard (CB) and Bogoliubov quasiparticle interference (QPI) modulations, which are considered to be characteristic features for the low-energy states around the antinodal and nodal regions of the Fermi surface, respectively, coexist in identical regions of the Cu-O plane. In the present work, these electronic superstructures are successfully separated from each other, and the local amplitude and phase are evaluated for the CB modulation and the $\boldsymbol{q}_1$ component of QPI, which are characterized by similar wave vectors. The $\boldsymbol{q}_1$-QPI component tends to be in-phase and antiphase with the CB modulation for positive and negative bias voltages, respectively. The significant spatial phase relationship is confirmed in regions where the local amplitude of CB modulation is comparatively large. This finding implies an interplay between the QPI and CB modulations.

DOI: 10.1103/PhysRevB.102.184513

I. INTRODUCTION

In high-T_c cuprate superconductors, various spectroscopic techniques have demonstrated interesting features for the electronic states around the Fermi level. Above all, scanning tunneling microscopy/spectroscopy (STM/STS) probing the local density of states (LDOS) on the atomic length scale has revealed that, in high-T_c cuprates such as $Bi_2Sr_2CaCu_2O_{8+x}$ (Bi2212), the electronic states form several kinds of superstructures, which are different depending on momentum and/or energy regions. On the nodal parts of the Fermi surface, the so-called "Fermi arcs," where a d-wave superconducting (SC) gap opens due to coherent pairing with its nodes located at the centers, interference occurs between the Bogoliubov quasiparticle states, leading to a spatial modulation in LDOS [1–9]. The quasiparticle interference (QPI) modulation consists of seven independent components characterized by dispersive wave vectors, $\boldsymbol{q}_1$−$\boldsymbol{q}_7$, changing in accordance with the corresponding QP energy.

On the other hand, on the antinodal parts outside the Fermi arcs, a pseudogap develops from around a temperature well above T_c and remains in the SC state [10–16]; it causes a suppression of DOS in an energy region larger than the SC gap around the Fermi level. In the antinodal region, the electronic states will be responsible for two superstructures, which are called the d-symmetry form factor density wave (dFF-DW) [17–22], coming from the pseudogap excitations, and checkerboard (CB) modulation [23–32], seemingly hosted by the residual states at energies similar to the SC gap or less. The CB modulation, which was observed in the SC state [23] and afterwards confirmed in the pseudogap state above T_c [24], runs along the two orthogonal Cu-O bond directions with an energy-independent period of ∼4a (a: Cu-O-Cu distance). The wave vector of CB modulation is similar to that of a QPI component $\boldsymbol{q}_1$. However, they have distinct dispersion relations. Another interesting feature for the CB modulation is that it tends to develop markedly around hole-doping level $p \sim 1/8$ in the underdoped region [29]. Recently, nanometer-resolution scanned Josephson tunneling microscopy (SJTM), performed in the SC state of optimally doped Bi2212, has detected a CB-like modulation of the Josephson critical current due to pair tunneling between the SC nanoflake STM tip and sample surface, suggesting the existence of a pair density wave (PDW) state [33–37] in high-T_c cuprates [38]. Therefore, whether such a PDW state can explain the CB modulation observed in the low-energy single-particle excitations is of considerable interest for a better understanding of cuprate superconductivity, as well.

As described above, the Fermi surface is roughly divided into nodal and antinodal regions, inside and outside the Fermi arc, in high-T_c cuprates. Such dichotomy of the Fermi surface [10–13,39–44] is one of the most striking features in their electronic systems. Thus far, angle-resolved photoemission spectroscopy has demonstrated that the nodal SC gap and the antinodal pseudogap are in a competitive relationship in the sense that these energy gaps take the Fermi surface from each other [11,12]. On the other hand, time-resolved pump-probe optical spectroscopy has suggested a clear time correlation between the recovery processes of the SC and pseudogap states. As these two states are completely destroyed and rather suppressed, respectively, in a region several tens of μm in diameter by a strong pump pulse, the recovery of the destroyed superconductivity seems to occur just after that of the suppressed pseudogap state [45]. Thus, it is still an open

*shuseimizuta@frontier.hokudai.ac.jp
†moda@sci.hokudai.ac.jp

question as to whether the electronic states in the antinodal region, responsible for the pseudogap and the electronic superstructures, are needless for or play an essential role in the SC mechanism.

In the present study, STM/STS experiments were performed at $T = 7$ K in underdoped Bi2212 with $p \sim 0.12$ and $T_c = 76$ K to investigate the spatial maps of differential conductance dI/dV, reflecting the LDOS, at low bias voltages or energies with respect to the Fermi level. We have succeeded in separating the CB and QPI modulations, which have been demonstrated to coexist in identical regions of the Cu-O plane, and simultaneously confirmed to be almost symmetric and antisymmetric for the sign change of bias voltage or single-particle excitation energy, respectively. Furthermore, the coexistence relationship between the CB and $\boldsymbol{q}_1$-QPI modulations was examined by analyzing their local amplitudes and phases. From the analyses, it was found that the CB modulation plays an effective role in settling the spatial phase of $\boldsymbol{q}_1$-QPI modulation. In light of this finding, we will discuss the origins of the CB and $\boldsymbol{q}_1$-QPI modulations and the possibility of an interplay between them.

II. EXPERIMENTAL PROCEDURES

Bi2212 single crystals were grown by the traveling solvent floating-zone method. The SC critical temperature T_c was determined from the diamagnetic transition curve. In STM/STS experiments, single crystals were cleaved *in situ* in an ultrahigh vacuum at 7 K just before moving the STM tip towards the sample surface. We performed STM imaging at low bias voltages on the order of 10 mV on the cleaved surfaces [46,47]. This is because such low bias STM imaging enables us to observe the Cu-O plane buried under the topmost Bi-O plane. In the present work, furthermore, the spatial dependence of differential conductance dI/dV is measured simultaneously in the process of low-bias STM imaging by using the following method: the bias voltage is modulated with a small amplitude while taking an STM current image by scanning the tip in constant height mode, and the output of a lock-in amplifier built into the measurement system, corresponding to dI/dV at the center value of applied bias voltage, is directly imaged, providing a dI/dV map. The details of low bias dI/dV imaging in constant height mode have been reported in Ref. [48].

III. RESULTS AND DISCUSSION

A. Coexistence of checkerboard and quasiparticle interference modulations

Figures 1(a) and 1(c) show low bias G ($\equiv dI/dV$) maps taken at 7 K on underdoped Bi2212 ($p \sim 0.12$ and $T_c = 76$ K) at sample bias voltages $V_s = +20$ and -20 mV, applied to the sample with respect to the STM tip. The magnitude of V_s is smaller than the value corresponding to the SC gap amplitude $\Delta_0 \sim 40$ meV at $p \sim 0.12$. In both maps, one can see a checkerboardlike electronic superstructure along the two orthogonal Cu-O bond directions, overlaid with the one-dimensional superlattice of the Bi-O plane. The details of the tunneling processes between the tip and the sample surface have been discussed in previous reports [48,49]. In the Fourier

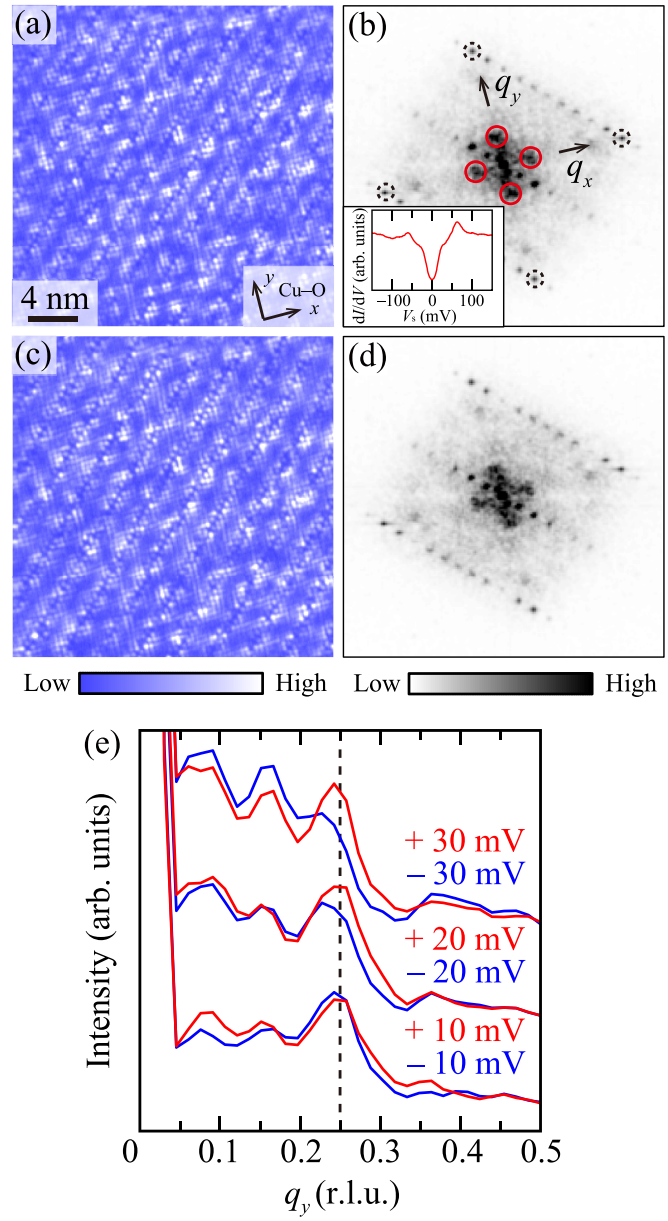

FIG. 1. $G(\boldsymbol{r}, V_s)$ maps measured at 7 K in underdoped Bi2212 with $p \sim 0.12$ and $T_c = 76$ K: (a) for $V_s = +20$ mV and (c) for $V_s = -20$ mV. The x and y axes (arrows) in (a) correspond to the Cu-O bond directions. FT maps of the $G(\boldsymbol{r}, V_s)$ maps: (b) for $V_s = +20$ mV and (d) for $V_s = -20$ mV. Solid and dashed circles indicate the Fourier spots corresponding to the electronic superstructure and the Bragg spots, respectively. The inset shows a typical example of dI/dV spectra measured in the same cleaved surface. It exhibits subgap structures at $|V_s| \sim 25$ mV within the spatially inhomogeneous pseudogap at larger energies. (e) Line cuts of the FT maps on the q_y axis plotted in a reciprocal lattice unit (r.l.u.) defined as $2\pi/a = 1$ for $V_s = \pm 10, \pm 20$, and ± 30 mV.

amplitude maps [Figs. 1(b) and 1(d)] [hereafter referred to as the Fourier transform (FT) maps] of $G(\boldsymbol{r}, V_s = \pm 20$ mV) maps, the spots corresponding to the superstructure are located around the origin. Figure 1(e) shows line cuts of the FT maps along the q_y axis from 0 to 0.5 in the scale as $2\pi/a = 1$ (a: lattice constant along the Cu-O directions or

Cu-O-Cu distance), together with the results for $V_s = \pm 30$ and ± 10 mV. One can see peaks around $q_y \sim 1/4$. The wave numbers of the Fourier components, roughly estimated from their peak positions, are almost independent of bias voltage. Such nondispersive behavior, which will be demonstrated more clearly in the last part of this subsection, is consistent with a characteristic feature of the CB modulation.

It is noteworthy that the intensities of $q_y \sim 1/4$ components on the line cuts are asymmetric with respect to the sign change of bias voltage. A similar behavior in the Fourier intensities has been observed in previous STM/STS studies on Bi2212, as well [30–32], and could be attributed to the so-called "setup effect," which has been considered to occur in the conventional method for dI/dV imaging [3,20,30]. However, the present dI/dV imaging, which can be done with the tip scanning in constant height mode under low bias voltages, is substantially free from the setup effect [50]. Therefore, the observed asymmetric behavior is intrinsic to the $q_y \sim 1/4$ component. This suggests the possibility that the CB modulation itself might be asymmetric for the inversion of bias polarity; i.e., the low-energy states in the antinodal region might have electron-hole asymmetry [31]. However, it has been pointed out for some cuprate superconductors that QPI patterns, including a component characterized by almost the same wave vector as the CB modulation, are also observed in their low-bias G maps [3,29], which prompts us to suppose that the coexistence of both electronic superstructures will cause the asymmetry in the intensity of the $q_y \sim 1/4$ component for the inversion of bias polarity. In fact, we will confirm below that the QPI modulation coexists with the CB modulation in $G(\boldsymbol{r}, V_s)$ maps.

Figure 2(a) shows a map of the ratios of $G(\boldsymbol{r}, \pm V_s)$ values at bias voltages of the opposite sign, defined as $Z(\boldsymbol{r}, V_s) \equiv G(\boldsymbol{r}, +V_s)/G(\boldsymbol{r}, -V_s)$ [3–5], for $V_s = +20$ mV. Since the spatial modulations in $G(\boldsymbol{r}, \pm V_s)$ maps are substantially smaller than their uniform backgrounds which are almost independent of bias polarity at least for the small voltages $|V_s| \leqslant 30$ mV studied, the spatial modulation in the $Z(\boldsymbol{r}, V_s)$ map will be proportional to that in a map defined as $G(\boldsymbol{r}, +V_s) - G(\boldsymbol{r}, -V_s)$. Therefore, in-phase and antiphase components in $G(\boldsymbol{r}, +V_s)$ and $G(\boldsymbol{r}, -V_s)$ maps are weakened and strengthened in the $Z(\boldsymbol{r}, V_s)$ map, respectively. Thus, little CB modulation, whose amplitude and phase are almost independent of bias polarity [23,48], is seen in the Z map [Fig. 2(a)]. On the other hand, the QPI components, whose phases have been considered to be reversed with the inversion of bias polarity [5], remain in the same Z map [3,4]. Actually, in the FT map [Fig. 2(b)], we can identify seven kinds of spots, marked $\boldsymbol{q}_1$–$\boldsymbol{q}_7$, corresponding to the seven independent QPI components. The line cut of the FT map along the q_y axis, the same direction as one of the CB wave vectors, is shown in Fig. 2(c), together with the results for other bias voltages. The Fourier peaks for the $\boldsymbol{q}_1$-QPI components are located near $q_y \sim 1/4$ or the wave number of the nondispersive CB. For each bias voltage, the wave vector $\boldsymbol{q}_{1y}$ of $\boldsymbol{q}_1$-QPI along the q_y axis was determined by the demodulation phase residue minimization technique [19], and the corresponding wave number is indicated by a bar in Fig. 2(c) for the line cuts. The wave number of $\boldsymbol{q}_1$-QPI is closest to that of the nondispersive CB at $|V_s| = 30$ mV and becomes larger away from it with the decrease of $|V_s|$. The $\boldsymbol{q}_1$-QPI modulation is weakly dispersive in contrast to the CB modulation.

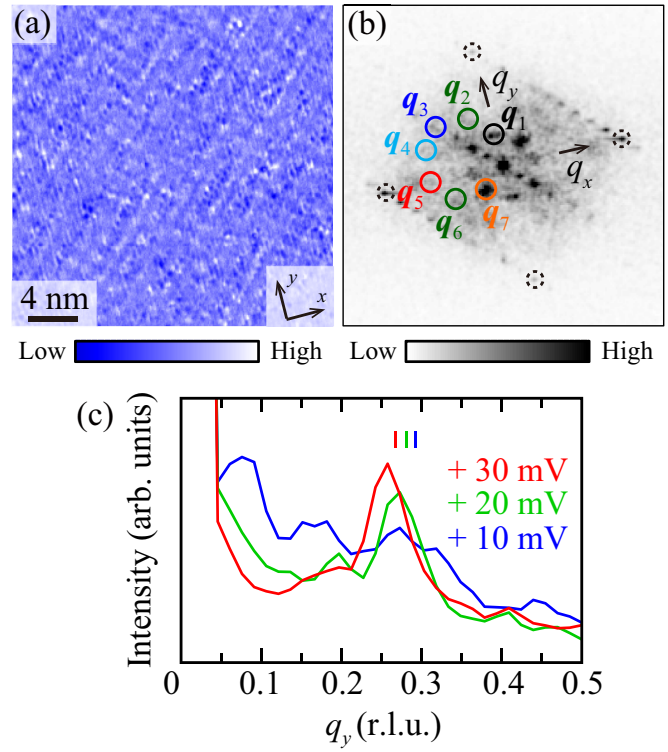

FIG. 2. (a) $Z(\boldsymbol{r}, V_s)$ map for $V_s = +20$ mV. (b) FT map of the $Z(\boldsymbol{r}, V_s)$ map for $V_s = +20$ mV. Solid circles indicate the Fourier spots corresponding to the seven independent components of QPI, $\boldsymbol{q}_1$–$\boldsymbol{q}_7$. (c) Line cuts of the FT maps on the q_y axis for $V_s = +10$, $+20$, and $+30$ mV. The position of each small bar indicates the wave number of weakly dispersive $\boldsymbol{q}_1$-QPI modulation $|\boldsymbol{q}_{1y}|$ determined by the demodulation phase residue minimization technique. For $V_s = +10$ mV, the demodulation phase residue has two minima, corresponding to two separated peaks near $q_y \sim 0.29$ in the line cut, and thus their mean wave vector was adopted as $\boldsymbol{q}_{1y}$.

As mentioned above, the QPI modulation can be extracted by making the Z map from low bias $G(\boldsymbol{r}, \pm V_s)$ maps including both the CB and QPI modulations. In the present study, to investigate the nature of each modulation by itself, we also extract the CB modulation from low bias $G(\boldsymbol{r}, \pm V_s)$ maps with their symmetrization. Then, we introduce an $S(\boldsymbol{r}, |V_s|)$ map defined as the following equation:

$$S(\boldsymbol{r}, |V_s|) \equiv \frac{G(\boldsymbol{r}, +V_s) + G(\boldsymbol{r}, -V_s)}{2}.$$

If the QPI modulation is antisymmetric for the inversion of bias polarity, it can be taken away by the symmetrization of $G(\boldsymbol{r}, \pm V_s)$. On the other hand, the almost symmetric CB modulation will remain in $S(\boldsymbol{r}, |V_s|)$ maps.

Figure 3 shows an $S(\boldsymbol{r}, |V_s|)$ map for $V_s = 20$ mV [Fig. 3(a)], its FT map [Fig. 3(b)], and the line cuts along the q_y axis on the FT maps for $|V_s| = 10$, 20, and 30 mV [Fig. 3(c)]. In the line cuts, one can see Fourier peaks around $q_y \sim 1/4$. Interestingly, the Fourier peak exhibits little dispersive behavior as expected; its central position seems to be

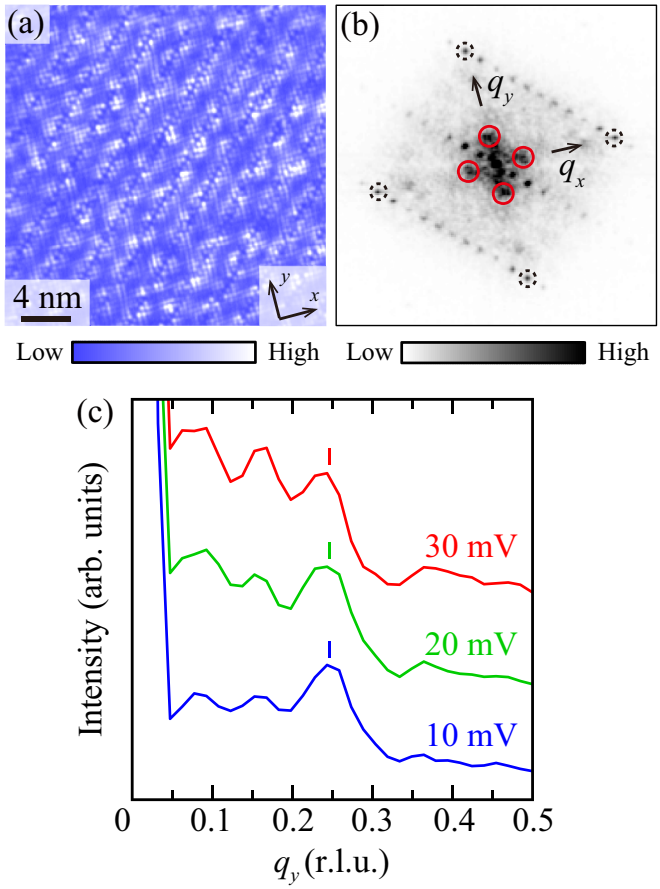

FIG. 3. (a) $S(\boldsymbol{r},\ |V_s|)$ maps for $|V_s| = 20$ mV. (b) FT maps of the $S(\boldsymbol{r},\ |V_s|)$ maps for $|V_s| = 20$ mV. Solid and dashed circles indicate the CB Fourier spots and the Bragg spots as in Fig. 1. (c) Line cuts of the FT maps on the q_y axis for $|V_s| = 10$, 20, and 30 mV. The position of each small bar indicates the wave number of CB modulation $|\boldsymbol{Q}_y|$ determined by the demodulation phase residue minimization technique.

unchanged for the bias voltages examined. Indeed, the wave vectors $\boldsymbol{Q}_y$ determined from the Fourier spots on the q_y axis by the demodulation phase residue minimization technique [19] are totally independent of bias voltage, as can be seen from the corresponding wave numbers indicated by bars in Fig. 3(c). This result is consistent with the nondispersive nature of CB modulation.

Furthermore, the comparison between the $G(\boldsymbol{r},\ V_s)$ and $S(\boldsymbol{r},\ |V_s|)$ maps [Figs. 1(a), 1(c), and 3(a)] indicates that the spatial pattern does not change largely before or after the subtraction of the QPI modulation; that is, the CB modulation is predominant in comparison to the QPI modulation. Thus, the present study confirms that the two modulations, which are characteristic features for the low-energy states of the Cu-O plane, coexist in identical regions, and are different in amplitude, dispersion relation, and symmetry for the sign change of energy with respect to the Fermi level.

B. Local amplitudes and phases of electronic superstructures

In the preceding subsection, the CB and QPI modulations were separated most satisfactorily. This enables us to investigate the local properties of each modulation by itself. First, let us evaluate the local amplitude and phase of CB modulation, focusing on the y direction (one of its propagation directions), with a method used in recent studies on the dFF-DW whose characteristic energy is of the order of the pseudogap, larger than that of the CB modulation [18]. For this purpose, we extract the CB modulation along the y direction, and construct its complex-valued analytic signal $S_{\boldsymbol{Q}_y}(\boldsymbol{r},\ |V_s|)$. The real part $\mathrm{Re}S_{\boldsymbol{Q}_y}(\boldsymbol{r},\ |V_s|)$ is obtained from an $S(\boldsymbol{r},\ |V_s|)$ map with the inverse FT of the corresponding complex-valued FT signals surrounding $\boldsymbol{q} = \boldsymbol{Q}_y$, which are cut out by multiplying a radial Gaussian-type mask function $e^{-(\boldsymbol{q}-\boldsymbol{Q}_y)^2/2\Lambda^2}$ for $|\boldsymbol{q} - \boldsymbol{Q}_y| \leqslant \sqrt{2\ln 2}\Lambda$ (half width at half maximum) ~ 0.05 and otherwise 0. Furthermore, the imaginary part $\mathrm{Im}S_{\boldsymbol{Q}_y}(\boldsymbol{r},\ |V_s|)$ is obtained in the same manner as $\mathrm{Re}S_{\boldsymbol{Q}_y}(\boldsymbol{r},\ |V_s|)$ except that its phase is delayed by $\pi/2$. The local amplitude $A^S_{\boldsymbol{Q}_y}(\boldsymbol{r},\ |V_s|)$ and phase $\varphi^S_{\boldsymbol{Q}_y}(\boldsymbol{r},\ |V_s|)$ are given by the following equations:

$$A^S_{\boldsymbol{Q}_y}(\boldsymbol{r},\ |V_s|) = \sqrt{\left[\mathrm{Re}S_{\boldsymbol{Q}_y}(\boldsymbol{r},\ |V_s|)\right]^2 + \left[\mathrm{Im}S_{\boldsymbol{Q}_y}(\boldsymbol{r},\ |V_s|)\right]^2}$$

and

$$\varphi^S_{\boldsymbol{Q}_y}(\boldsymbol{r},\ |V_s|) = \arctan\left[\mathrm{Im}S_{\boldsymbol{Q}_y}(\boldsymbol{r},\ |V_s|)/\mathrm{Re}S_{\boldsymbol{Q}_y}(\boldsymbol{r},\ |V_s|)\right].$$

Figures 4(a), 4(c), and 4(e) are maps of the local amplitude of CB modulation $A^S_{\boldsymbol{Q}_y}(\boldsymbol{r},\ |V_s|)$ at $|V_s| = 30$, 20, and 10 mV, respectively. First of all, one can see in these figures that the spatial dependence of $A^S_{\boldsymbol{Q}_y}(\boldsymbol{r},\ |V_s|)$ is almost independent of bias voltage. Furthermore, the local amplitude of CB modulation is spatially inhomogeneous on the nanometer scale. There are some regions where its development is relatively strong regardless of bias voltage. On the other hand, Figs. 4(b), 4(d), and 4(f) are maps of the local phase of CB modulation $\varphi^S_{\boldsymbol{Q}_y}(\boldsymbol{r},\ |V_s|)$ at $|V_s| = 30$, 20, and 10 mV, respectively. The spatial dependence of $\varphi^S_{\boldsymbol{Q}_y}(\boldsymbol{r},\ |V_s|)$ is almost independent of bias voltage, like that of $A^S_{\boldsymbol{Q}_y}(\boldsymbol{r},\ |V_s|)$. In these figures, one can see some edge dislocations; an extra single period is inserted into the nondistorted ideal CB lattice like a wedge towards the so-called "dislocation cores" marked by black dots. Interestingly, the local amplitude of CB modulation tends to zero at such dislocation cores. Furthermore, it was confirmed in the present study that topological defectlike behavior is observed at the dislocation cores, each of which has a $+2\pi$ or -2π phase winding around itself in the phase field demodulated by regarding $\boldsymbol{Q}_y$ as a reference wave vector. These properties for the local amplitude and phase of CB modulation, including their relationship, are similar to those reported for the pseudogap energy scale superstructure to be consistent with topological defects in smectic modulations [22].

Second, we focus on the $\boldsymbol{q}_1$ component of QPI modulation, whose wave vector is close to that of CB modulation, to understand their coexistence relationship. Figure 5 shows maps of the local amplitude $A^Z_{\boldsymbol{q}_{1y}}(\boldsymbol{r},\ V_s)$ and phase $\varphi^Z_{\boldsymbol{q}_{1y}}(\boldsymbol{r},\ V_s)$ of the $\boldsymbol{q}_1$-QPI component along the y direction. These maps were

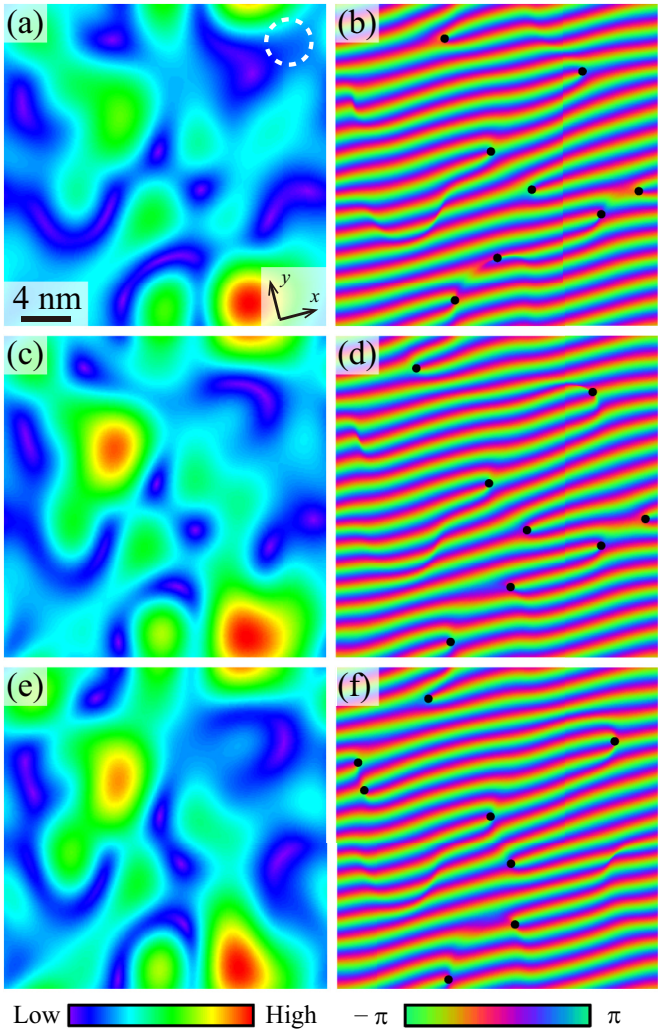

FIG. 4. Maps of the local amplitude and phase for the y-direction component of CB modulation; the left and right columns are for the local amplitude and phase, respectively, and show their results for $|V_s| = 30$ mV (a), (b), 20 mV (c), (d), and 10 mV (e), (f) in order from the top. The dashed circle in (a) indicates the coarse graining length scale. Black dots in the local phase maps indicate edge dislocation cores.

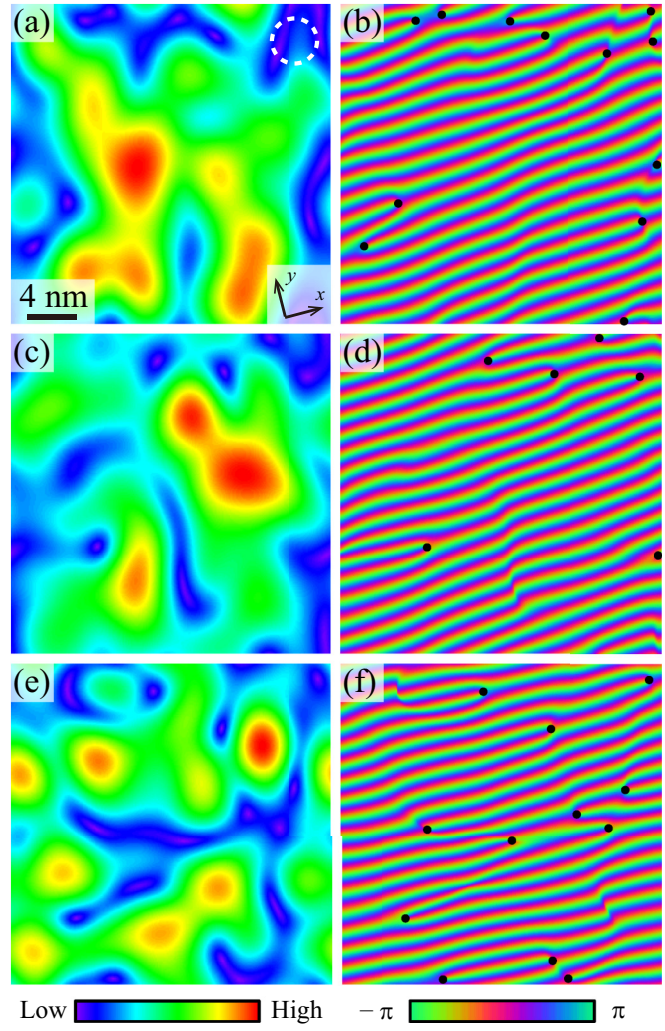

FIG. 5. Maps of the local amplitude and phase for the y-direction component of $\boldsymbol{q}_1$-QPI modulation; the left and right columns are for the local amplitude and phase, respectively, and show the results for $V_s = +30$ mV (a), (b), +20 mV (c), (d), and +10 mV (e), (f). Black dots in the local phase maps indicate edge dislocation cores as in Fig. 4.

obtained by using the $Z(\boldsymbol{r},\ V_s)$ maps in a way similar to the case of CB modulation;

$$A^Z_{\boldsymbol{q}_{1y}}(\boldsymbol{r},\ V_s) = \sqrt{\left[\mathrm{Re}Z_{\boldsymbol{q}_{1y}}(\boldsymbol{r},\ V_s)\right]^2 + \left[\mathrm{Im}Z_{\boldsymbol{q}_{1y}}(\boldsymbol{r},\ V_s)\right]^2}$$

and

$$\varphi^Z_{\boldsymbol{q}_{1y}}(\boldsymbol{r},\ V_s) = \arctan\left[\mathrm{Im}Z_{\boldsymbol{q}_{1y}}(\boldsymbol{r},\ V_s)/\mathrm{Re}Z_{\boldsymbol{q}_{1y}}(\boldsymbol{r},\ V_s)\right].$$

The local amplitude of $\boldsymbol{q}_1$-QPI component $A^Z_{\boldsymbol{q}_{1y}}(\boldsymbol{r},\ V_s)$ is strongly inhomogeneous on the nanometer scale as in the CB modulation. However, the amplitude inhomogeneity of $\boldsymbol{q}_1$-QPI component has different energy dependence from the case of CB modulation. For the $\boldsymbol{q}_1$-QPI component, it changes dramatically with decreasing energy, as shown in the left column of Fig. 5. The local phase of the $\boldsymbol{q}_1$-QPI component $\varphi^Z_{\boldsymbol{q}_{1y}}(\boldsymbol{r},\ V_s)$, shown in the right column, strongly depends on energy as well. One can see that the wavelength, the interval between neighboring equivalent phase lines, gradually becomes shorter with lowering bias voltage, reflecting its weak energy dependence. Furthermore, edge dislocation cores in $\varphi^Z_{\boldsymbol{q}_{1y}}(\boldsymbol{r},\ V_s)$, marked by black dots, at which the local amplitude $A^Z_{\boldsymbol{q}_{1y}}(\boldsymbol{r},\ V_s)$ tends to zero, are confirmed as in the CB modulation. However, for $\boldsymbol{q}_1$-QPI, the number and position of dislocation cores change with energy in accordance with the energy-dependent inhomogeneity of $A^Z_{\boldsymbol{q}_{1y}}(\boldsymbol{r},\ V_s)$. This finding clearly shows that the CB and $\boldsymbol{q}_1$-QPI modulations are distinct in terms of the presence or absence of energy dependence in the inhomogeneous local amplitude and phase as well.

C. Relationship between checkerboard and quasiparticle interference modulations

To discuss the spatial relationship between the nondispersive CB and weakly dispersive $\boldsymbol{q}_1$-QPI modulations, we

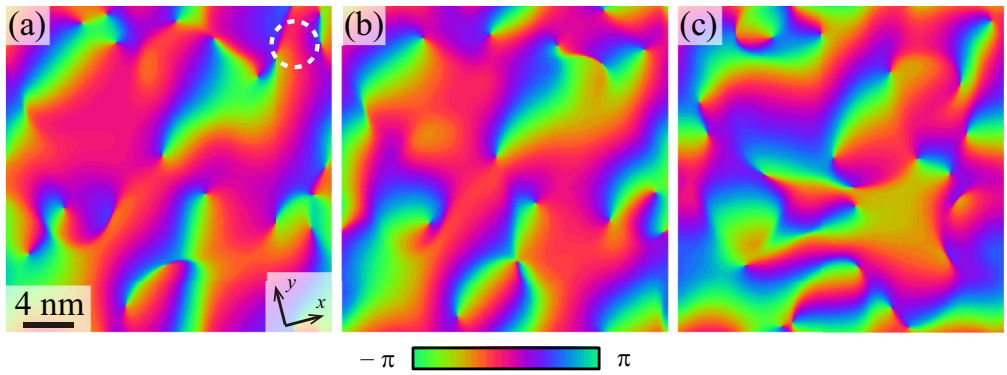

FIG. 6. Local phase difference between the CB and $\boldsymbol{q}_1$-QPI modulations; (a)–(c) are for $V_s = +30$, $+20$, and $+10$ mV, respectively.

introduce maps of the difference between their local phases, defined as follows:

$$\Delta\varphi(\boldsymbol{r},\ V_s) \equiv \varphi^S_{\boldsymbol{Q}_y}(\boldsymbol{r},\ |V_s|) - \varphi^Z_{\boldsymbol{q}_{1y}}(\boldsymbol{r},\ V_s),$$

where $-\pi \leqslant \Delta\varphi(\boldsymbol{r},\ V_s) \leqslant \pi$. The map of $\Delta\varphi(\boldsymbol{r},\ V_s)$ is shown for $V_s = +30$, $+20$, and $+10$ mV in Fig. 6. For $V_s = +30$ mV, where the wave number of $\boldsymbol{q}_1$-QPI is closest to that of CB [see Figs. 2(c) and 3(c)], the local phase difference $\Delta\varphi(\boldsymbol{r},\ V_s)$ takes on values around 0 in a comparatively large area, indicating that the spatial phases of CB and $\boldsymbol{q}_1$-QPI tend to match locally on the nanometer scale, although there is a finite difference in their global wave numbers. The degree of local phase matching gradually becomes lower, accompanied with the reduction of $\boldsymbol{q}_1$-QPI intensity, as the wave number of $\boldsymbol{q}_1$-QPI goes away from that of CB with the lowering of V_s (Fig. 6). This behavior can also be confirmed in the histogram of $\Delta\varphi(\boldsymbol{r},\ V_s)$, as shown in Fig. 7(a).

From a comparison between the $\Delta\varphi(\boldsymbol{r},\ V_s)$ and $A^S_{\boldsymbol{Q}_y}(\boldsymbol{r},\ |V_s|)$ maps for $V_s = +30$ and $+20$ mV (Fig. 4), it can be suggested that the local phase matching tends to occur where the CB modulation develops well. This suggestion is supported by analyses on the normalized cross-correlation coefficient of $A^S_{\boldsymbol{Q}_y}(\boldsymbol{r},\ |V_s|) - \langle A^S_{\boldsymbol{Q}_y}(\boldsymbol{r},\ |V_s|)\rangle$ and $|\Delta\varphi(\boldsymbol{r},\ V_s)| - \pi/2$ [Fig. 7(b)]. Here, $\langle A^S_{\boldsymbol{Q}_y}(\boldsymbol{r},\ |V_s|)\rangle$ is the spatial average of $A^S_{\boldsymbol{Q}_y}(\boldsymbol{r},\ |V_s|)$, and the one-dimensional cross-correlation coefficient as a function of distance is obtained by radially averaging the two-dimensional one. A negative correlation between the two quantities is clearly observed for $V_s = +30$ and $+20$ mV, although such a correlation is unclear for $V_s = +10$ mV. This result indicates that for the former two cases in which the wave number of $\boldsymbol{q}_1$-QPI is relatively closer to that of CB, the phase difference $\Delta\varphi(\boldsymbol{r},\ V_s)$ tends to take on values around 0 where the local amplitude of CB modulation becomes large. Additionally, similar analyses on the cross correlation between $A^S_{\boldsymbol{Q}_y}(\boldsymbol{r},\ |V_s|) - \langle A^S_{\boldsymbol{Q}_y}(\boldsymbol{r},\ |V_s|)\rangle$ and $A^Z_{\boldsymbol{q}_{1y}}(\boldsymbol{r},\ V_s) - \langle A^Z_{\boldsymbol{q}_{1y}}(\boldsymbol{r},\ V_s)\rangle$ have demonstrated that the amplitudes of CB and $\boldsymbol{q}_1$-QPI exhibit a clear positive correlation at least for $V_s = +30$ mV where the wave number of $\boldsymbol{q}_1$-QPI is closest to that of CB [Fig. 7(c)]. These findings suggest that the CB modulation plays an effective role in settling the spatial phase of $\boldsymbol{q}_1$-QPI modulation.

It should be added that the present finding on the spatial phase relationship between the CB and $\boldsymbol{q}_1$-QPI modulations, discussed above for positive bias voltages, also provides a convincing explanation for the Fourier intensities around $q_y = 1/4$ which are asymmetric with respect to the sign change of bias voltage [Fig. 1(e)]. As mentioned in Sec. III A, the phase

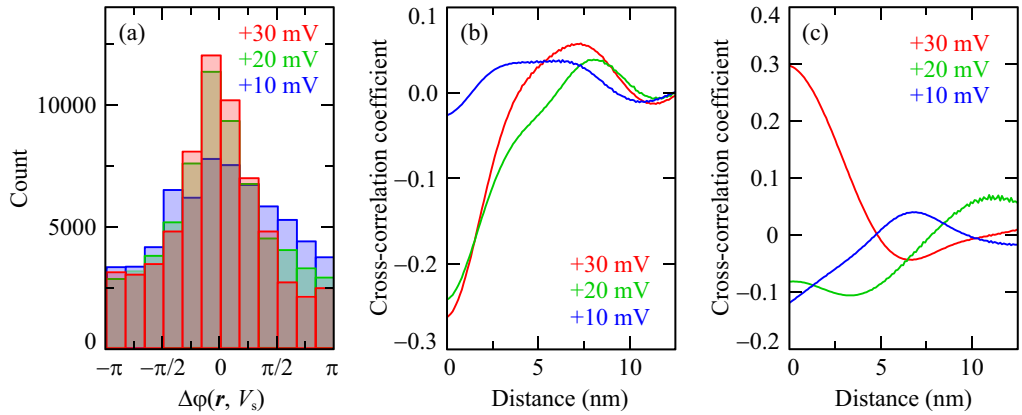

FIG. 7. (a) Histograms of the local phase difference between the CB and $\boldsymbol{q}_1$-QPI modulations for $V_s = +30$, $+20$, and $+10$ mV. Radially averaged cross-correlation coefficients as a function of distance: (b) for $A^S_{\boldsymbol{Q}_y}(\boldsymbol{r},\ |V_s|) - \langle A^S_{\boldsymbol{Q}_y}(\boldsymbol{r},\ |V_s|)\rangle$ and $|\Delta\varphi(\boldsymbol{r},\ V_s)| - \pi/2$ and (c) for $A^S_{\boldsymbol{Q}_y}(\boldsymbol{r},\ |V_s|) - \langle A^S_{\boldsymbol{Q}_y}(\boldsymbol{r},\ |V_s|)\rangle$ and $A^Z_{\boldsymbol{q}_{1y}}(\boldsymbol{r},\ V_s) - \langle A^Z_{\boldsymbol{q}_{1y}}(\boldsymbol{r},\ V_s)\rangle$.

difference between the positive and negative bias $\boldsymbol{q}_1$-QPI modulations is $\sim\pi$. Therefore, the CB and $\boldsymbol{q}_1$-QPI modulations tend to be nearly in-phase and antiphase with each other for positive and negative bias voltages, respectively. This leads to the constructive and destructive effects of the two electronic superstructures on the LDOS, causing the asymmetric Fourier intensities around $q_y \sim 1/4$.

A possible explanation for the role of CB modulation in the $\boldsymbol{q}_1$-QPI phase settling is that the region wherein the CB modulation develops markedly would serve as an effective scattering medium for Bogoliubov QPs on parts of the Fermi arc leading to the $\boldsymbol{q}_1$ component. It has been demonstrated that the coherence factor in determining the probability of QP scatterings between states connected by $\boldsymbol{q}_i$ depends on the nature of the scatterer and whether the sign of the d-wave SC gap is preserved or not between their QP states [6]. In the case of $\boldsymbol{q}_1$, which preserves the sign of the d-wave SC gap, the coherence factor is strongly suppressed for weak scalar potential scattering, while it takes a finite value for resonant or Andreev scattering. Recently, it has been suggested in STM/STS experiments, including SJTM in optimally doped Bi2212, that the superconductivity may coexist with a pair density wave (PDW) and/or a charge density wave accompanied by PDW [32,38,51], which has also been predicted by some theoretical studies [35–37]. Furthermore, the present study also suggests that the $\boldsymbol{q}_1$-QPI tends to be marked as the corresponding states approach the edges of Fermi arcs or the so-called "hot spots," which have been pointed out to be responsible for the density waves [35,36,52]. If the CB modulation observed in the low-energy single-particle excitations arises from such an electronic order, it could provide a pair potential spatially modulated in the amplitude, causing the Andreev scattering of QPs reasonable for the $\boldsymbol{q}_1$ component of their interference. However, in underdoped Bi2212, the spatial modulation of the energy gap ascribed to the CB formation, which would reflect the pair potential, remains unclear, and therefore the question of whether the CB modulation can serve as an Andreev scattering medium for Bogoliubov QPs is still open to discussion. In any case, the present results on their coexistence relationship seem to indicate an interplay between the CB and QPI modulations.

IV. SUMMARY

In the present STM/STS study in the SC state of $p \sim 0.12$ underdoped Bi2212, we performed dI/dV imaging in the process of taking an STM current image in constant height mode at a low bias voltage in the range of $|V_s| \leqslant 30$ mV, and demonstrated the coexistence of CB and QPI modulations in identical regions of the Cu-O plane. These electronic superstructures were successfully separated from each other, which enabled us to evaluate the local amplitude and phase of each modulation by itself. For both the CB and $\boldsymbol{q}_1$-QPI modulations characterized by similar wave vectors, the local amplitude exhibits spatial inhomogeneity, and tends to zero at edge dislocation cores in the local phase. However, the CB and $\boldsymbol{q}_1$-QPI modulations are distinct in terms of the absence or presence of energy dependence in the inhomogeneous local amplitude and phase, which are little and strongly energy dependent for the former and the latter, respectively. Furthermore, it was found that the CB modulation plays an effective role in settling the spatial phase of $\boldsymbol{q}_1$-QPI modulation. This finding implies an interplay between the QPI and CB modulations, which seem to be characteristic features for the low-energy states around the nodal and antinodal regions of the Fermi surface, respectively.

ACKNOWLEDGMENTS

The authors would like to thank T. Kurosawa and Y. Toda for valuable comments and discussions. The present work was supported in part by JSPS KAKENHI Grant No. 19K03732. This research was also supported in part by Hokkaido University, Global Facility Center (GFC), Advanced Physical Property Open Unit (APPOU), funded by MEXT under "Support Program for Implementation of New Equipment Sharing System" (Grant No. JPMXS0420100318).

[1] J. E. Hoffman, K. McElroy, D.-H. Lee, K. M. Lang, H. Eisaki, S. Uchida, and J. C. Davis, Science **297**, 1148 (2002).
[2] K. McElroy, R. W. Simmonds, J. E. Hoffman, D.-H. Lee, K. J. Orenstein, H. Eisaki, S. Uchida, and J. C. Davis, Nature (London) **422**, 592 (2003).
[3] T. Hanaguri, Y. Kohsaka, J. C. Davis, C. Lupien, I. Yamada, M. Azuma, M. Takano, K. Ohishi, M. Ono, and H. Takagi, Nat. Phys. **3**, 865 (2007).
[4] Y. Kohsaka, C. Taylor, P. Wahl, A. Schmidt, J. Lee, K. Fujita, J. W. Alldredge, K. McElroy, J. Lee, H. Eisaki, S. Uchida, D.-H. Lee, and J. C. Davis, Nature (London) **454**1072 (2008).
[5] K. Fujita, I. Grigorenko, J. Lee, W. Wang, J. X. Zhu, J. C. Davis, H. Eisaki, S. Uchida, and A. V. Balatsky, Phys. Rev. B **78**, 054510 (2008).
[6] M. Maltseva and P. Coleman, Phys. Rev. B **80**, 144514 (2009).
[7] M. F. Crommie, C. P. Lutz, and D. M. Eigler, Nature (London) **363**, 524 (1993).
[8] Y. Hasegawa and Ph. Avouris, Phys. Rev. Lett. **71**, 1071 (1993).
[9] J.-X. Yin, S. S. Zhang, H. Li, K. Jiang, G. Chang, B. Zhang, B. Lian, C. Xiang, I. Belopolski, H. Zheng, T. A. Cochran, S.-Y. Xu, G. Bian, K. Liu, T.-R. Chang, H. Lin, Z.-Y. Lu, Z. Wang, S. Jia, W. Wang, and M. Z. Hasan, Nature (London) **562**, 91 (2018).
[10] M. R. Norman, H. Ding, M. Randeria, J. C. Campuzano, T. Yokoya, T. Takeuchi, T. Takahashi, T. Mochiku, K. Kadowaki, P. Guptasarma, and D. G. Hinks, Nature (London) **392**, 157 (1998).
[11] K. Tanaka, W. S. Lee, D. H. Lu, A. Fujimori, T. Fujii, Risdiana, I. Terasaki, D. J. Scalapino, T. P. Devereaux, Z. Hussain, and Z.-X. Shen, Science **314**, 1910 (2006).
[12] T. Kondo, T. Takeuchi, A. Kaminski, S. Tsuda, and S. Shin, Phys. Rev. Lett. **98**, 267004 (2007).
[13] T. Yoshida, M. Hashimoto, S. Ideta, A. Fujimori, K. Tanaka, N. Mannella, Z. Hussain, Z.-X. Shen, M. Kubota, K. Ono, S. Komiya, Y. Ando, H. Eisaki, and S. Uchida, Phys. Rev. Lett. **103**, 037004 (2009).

[14] I. Madan, T. Kurosawa, Y. Toda, M. Oda, T. Mertelj, and D. Mihailovic, Nat. Commun. **6**, 6958 (2015).
[15] R. M. Dipasupil, M. Oda, N. Momono, and M. Ido, J. Phys. Soc. Jpn. **71**, 1535 (2002).
[16] Y. H. Liu, Y. Toda, K. Shimatake, N. Momono, M. Oda, and M. Ido, Phys. Rev. Lett. **101**, 137003 (2008).
[17] K. Fujita, M. H. Hamidian, S. D. Edkins, C. K. Kim, Y. Kohsaka, M. Azuma, M. Takano, H. Takagi, H. Eisaki, S. Uchida, A. Allais, M. J. Lawler, E.-A. Kim, S. Sachdev, and J. C. Davis, Proc. Natl. Acad. Sci. USA **111**, E3026 (2014).
[18] M. H. Hamidian, S. D. Edkins, C. K. Kim, J. C. Davis, A. P. Mackenzie, H. Eisaki, S. Uchida, M. J. Lawler, E.-A. Kim, S. Sachdev, and K. Fujita, Nat. Phys. **12**, 150 (2016).
[19] A. Mesaros, K. Fujita, S. D. Edkins, M. H. Hamidian, H. Eisaki, S. Uchida, J. C. Davis, M. J. Lawler, and E.-A. Kim, Proc. Natl. Acad. Sci. USA **113**, 12661 (2016).
[20] Y. Kohsaka, C. Taylor, K. Fujita, A. Schmidt, C. Lupien, T. Hanaguri, M. Azuma, M. Takano, H. Eisaki, H. Takagi, S. Uchida, and J. C. Davis, Science **315**, 1380 (2007).
[21] M. J. Lawler, K. Fujita, J. Lee, A. R. Schmidt, Y. Kohsaka, C. K. Kim, H. Eisaki, S. Uchida, J. C. Davis, J. P. Sethna, and E.-A. Kim, Nature (London) **466**, 347 (2010).
[22] A. Mesaros, K. Fujita, H. Eisaki, S. Uchida, J. C. Davis, S. Sachdev, J. Zaanen, M. J. Lawler, and E.-A. Kim, Science **333**, 426 (2011).
[23] C. Howald, H. Eisaki, N. Kaneko, M. Greven, and A. Kapitulnik, Phys. Rev. B **67**, 014533 (2003).
[24] M. Vershinin, S. Misra, S. Ono, Y. Abe, Y. Ando, and A. Yazdani, Science **303**, 1995 (2004).
[25] T. Hanaguri, C. Luplen, Y. Kohsaka, D.-H. Lee, M. Azuma, M. Takano, H. Takagi, and J. C. Davis, Nature (London) **430**, 1001 (2004).
[26] K. McElroy, D.-H. Lee, J. E. Hoffman, K. M. Lang, J. Lee, E. W. Hudson, H. Eisaki, S. Uchida, and J. C. Davis, Phys. Rev. Lett. **94**, 197005 (2005).
[27] N. Momono, A. Hashimoto, Y. Kobatake, M. Oda, and M. Ido, J. Phys. Soc. Jpn. **74**, 2400 (2005).
[28] T. Machida, Y. Kamijo, K. Harada, T. Noguchi, R. Saito, T. Kato, and H. Sakata, J. Phys. Soc. Jpn. **75**, 083708 (2006).
[29] C. V. Parker, P. Aynajian, E. H. da Silva Neto, A. Pushp, S. Ono, J. Wen, Z. Xu, G. Gu, and Ali Yazdani, Nature (London) **468**, 677 (2010).
[30] J. W. Alldredge, K. Fujita, H. Eisaki, S. Uchida, and K. McElroy, Phys. Rev. B **85**, 174501 (2012).
[31] E. H. da Silva Neto, P. Aynajian, A. Frano, R. Comin, E. Schierle, E. Weschke, A. Gyenis, J. Wen, J. Schneeloch, Z. Xu, S. Ono, G. Gu, M. Le Tacon, and A. Yazdani, Science **343**, 393 (2014).
[32] W. Ruan, X. Li, C. Hu, Z. Hao, H. Li, P. Cai, X. Zhou, D.-H. Lee, and Y. Wang, Nat. Phys. **14**, 1178 (2018).
[33] E. Fradkin, S. A. Kivelson, and J. M. Tranquada, Rev. Mod. Phys. **87**, 457 (2015).
[34] D. F. Agterberg, J.C. Davis, S. D. Edkins, E. Fradkin, D. J. V. Harlingen, S. A. Kivelson, P. A. Lee, L. Radzihovsky, J. M. Tranquada, and Y. Wang, Annu. Rev. Condens. Matter Phys. **11**, 231 (2020).
[35] Y. Wang, D. F. Agterberg, and A. Chubukov, Phys. Rev. B **91**, 115103 (2015).
[36] Y. Wang, D. F. Agterberg, and A. Chubukov, Phys. Rev. Lett. **114**, 197001 (2015).
[37] P. A. Lee, Phys. Rev. X **4**, 031017 (2014).
[38] M. H. Hamidian, S. D. Edkins, S. H. Joo, A. Kostin, H. Eisaki, S. Uchida, M. J. Lawler, E.-A. Kim, A. P. Mackenzie, K. Fujita, J. Lee, and J. C. Davis, Nature (London) **532**, 343 (2016).
[39] D. Pines, Physica C **282**, 273 (1997); Z. Phys. B **103**, 129 (1997).
[40] X.-G. Wen and P. A. Lee, Phys. Rev. Lett. **80**, 2193 (1998).
[41] V. B. Geshkenbein, L. B. Ioffe, and A. I. Larkin, Phys. Rev. B **55**, 3173 (1997).
[42] N. Furukawa, T. M. Rice, and M. Salmhofer, Phys. Rev. Lett. **81**, 3195 (1998).
[43] M. Oda, R. M. Dipasupil, N. Momono, and M. Ido, J. Phys. Soc. Jpn. **69**, 983 (2000).
[44] T. Kurosawa, N. Momono, M. Oda, and M. Ido, Phys. Rev. B. **85**, 134522 (2012).
[45] Y. Toda, T. Mertelj, P. Kusar, T. Kurosawa, M. Oda, M. Ido, and D. Mihailovic, Phys. Rev. B **84**, 174516 (2011).
[46] A. Hashimoto, N. Momono, M. Oda, and M. Ido, Phys. Rev. B **74**, 064508 (2006).
[47] T. Kurosawa, T. Yoneyama, Y. Takano, M. Hagiwara, R. Inoue, N. Hagiwara, K. Kurusu, K. Takeyama, N. Momono, M. Oda, and M. Ido, Phys. Rev. B **81**, 094519 (2010).
[48] T. Kurosawa, K. Takeyama, S. Baar, Y. Shibata, M. Kataoka, S. Mizuta, H. Yoshida, N. Momono, M. Oda, and M. Ido, J. Phys. Soc. Jpn. **85**, 044709 (2016).
[49] I. Martin, A.V. Balatsky, and J. Zaanen, Phys. Rev. Lett. **88**, 097003 (2002).
[50] A. J. Macdonald, Y.-S. Tremblay-Johnston, S. Grothe, S. Chi1, P. Dosanjh, S. Johnston, and S. A. Burke, Nanotechnology **27**, 414004 (2016).
[51] Z. Du, H. Li, S. H. Joo, E. P. Donoway, J. Lee, J. C. Davis, G. Gu, P. D. Johnson, and K. Fujita, Nature (London) **580**, 65 (2020).
[52] R. Comin, A. Frano, M. M. Yee, Y. Yoshida, H. Eisaki, E. Schierle, E. Weschke, R. Sutarto, F. He, A. Soumyanarayanan, Y. He, M. L. Tacon, I. S. Elfimov, J. E. Hoffman, G. A. Sawatzky, B. Keimer, and A. Damascelli, Science **343**, 390 (2014).

Correction: The previously published Figures 7(b) and 7(c) contained incorrect axis scales and have been replaced.